Modeling of peritectic coupled growth in Cu–Sn alloys

J. Valloton [a], J.A. Dantzig [a,b,*], M. Plapp [c], M. Rappaz [a]

[a] *Computational Materials Laboratory, Institute of Materials, Ecole Polytechnique Fédérale de Lausanne, Station 12, CH-1015 Lausanne, Switzerland*
[b] *Mechanical Science and Engineering, University of Illinois, Urbana, IL 61801, USA*
[c] *Physique de la Matière Condensée, Ecole Polytechnique, CNRS, 91128 Palaiseau, France*

Abstract

In directional solidification experiments on hypoperitectic Cu–Sn alloys at low velocity and high thermal gradient, both lamellar and fibrous coupled peritectic growth patterns have been observed. Two phenomena that had not been observed in previous experiments on other alloy systems are investigated here with the help of different modeling approaches. The mean volume fraction of primary phase α, $\bar{g}_\alpha$, as determined by X-ray microtomography, decreases with solidification distance over the entire length of the coupled zone, but is always much larger than that expected from the equilibrium phase diagram. Moreover, oscillations in $\bar{g}_\alpha$ with a spatial periodicity approximately equal to the lamellar spacing are also observed. The first observation is explained semi-quantitatively by a simple 1D diffusion model, which reveals that the onset of coupled growth occurs during the initial transient of the primary phase planar front growth. A two-dimensional phase-field model is used to monitor the subsequent microstructure evolution, and shows that the lamellar structure exhibits collective 1-λ oscillations. In agreement with previous studies, it was found that these oscillations lead to stable coupled growth only for a limited range of the control parameters.
© 2013 Acta Materialia Inc. Published by Elsevier Ltd. All rights reserved.

Keywords: Peritectic solidification; Directional solidification; Phase field; Copper alloys; Coupled growth

1. Introduction

Peritectics represent an important class of industrial alloys, including steels, brasses and bronzes. These alloys show a wide variety of microstructures in directional solidification at low speed [1–13], including regions of primary α, primary β, islands of one phase in the other and coupled growth. It is this latter microstructure that is of most interest here.

In contrast to eutectic coupled growth, which is widely observed in all eutectic alloys and appears under a large range of growth conditions, peritectic coupled growth had long remained elusive, although its possibility was predicted quite a long time ago [14,15]. Several conditions for its appearance have now been clarified. First, the solidifica-tion velocity must be below the threshold for morphological instability for both solid phases to avoid the formation of dendrites or cells. Second, convection has a much larger effect in peritectics than in eutectics, because the growth rate is usually much lower in peritectics, and thus even a very small amount of convection can lead to the appearance of new two-phase microstructures [16]; truly diffusive coupled growth can therefore only be expected in systems in which convection is absent or at least of low intensity. Finally, it was found in experiments and by boundary integral simulations on the Fe–Ni system that coupled growth is stable only in certain ranges of concentrations and lamellar spacings [10]; at the boundary of this range, stable limit cycles of 1-λ oscillations around the steady state were observed. Because of the limited stability, the initiation of coupled growth requires a non-trivial dynamical process, which generally leads to long transients before coupled growth emerges [8,17]. Since it is at present unknown how the stability conditions and the dynamics of the tran-

* Corresponding author at: Mechanical Science and Engineering, University of Illinois, Urbana, IL 61801, USA. Tel.: +1 2173334107.
E-mail address: dantzig@illinois.edu (J.A. Dantzig).

sient depend on the characteristics of the phase diagram, more information on the initiation and stability of coupled growth in other alloy systems is needed.

We focus on hypoperitectic tin bronze, corresponding to the composition range 13.5–22 wt.% Sn. In a previous article [18], we presented the results of X-ray tomographic microscopy studies on a Cu–21 wt.% Sn alloy that had been directionally solidified in a fixed temperature gradient $G_\ell \approx 21$ K mm^{-1} at a constant pulling speed $v_p = 0.58$ μm s^{-1}. Here, we present further experimental results for $v_p = 0.38$ μm s^{-1}. In contrast to the results reported in Ref. [11], the specimens used here were cylinders of 0.5 mm diameter. This diameter is small enough that solutal buoyancy-induced convection is considerably reduced. The resulting microstructure, described more thoroughly in Section 2, showed an initial transient of primary α-phase, followed by an extended region of lamellar and/or fibrous coupled growth of α and β. The detailed analysis of this two-phase region using X-ray tomography revealed several phenomena that have not been reported in experiments on other peritectic alloy systems. These include:

- The volume fraction of primary phase, g_α, oscillates along the length of the sample, with a spatial period approximately equal to the average lamellar spacing.
- The mean value of g_α, $\bar{g}_\alpha$, decreases as coupled growth proceeds, but always remains much larger than expected from the equilibrium phase diagram.

The goal of the present paper is to better understand these observations with the help of suitable models.

Concerning the second point, the qualitative reasons for the differences between the present observations and previous experiments are fairly simple. As already mentioned above, coupled lamellar growth should be expected only when the pulling speed is below the threshold for the Mullins–Sekerka instability in either the primary or peritectic phase. Therefore, observations of peritectic coupled growth are easier to make in alloys with small freezing range, since larger pulling speeds can be used (e.g. Refs. [8,9] on Fe–Ni used $v_p \sim 10$ μm s^{-1}). The Cu–Sn alloy, in contrast, has a large freezing range, and thus requires much smaller pulling speeds to ensure morphological stability. For the pulling speeds used here, the diffusion length D_ℓ/v_p, where D_ℓ is the solute diffusion coefficient in the liquid, is of the order 10 mm. It is also known that the transient that leads from the initial equilibrium interface at the liquidus temperature to the steady-state interface at the solidus temperature (the "recoil" of the interface) takes several times the diffusion time D_ℓ/v_p^2 [19]. Therefore, this transient would extend over a solidification distance of several centimeters and last for several hours if only the α-phase were to grow.

When the interface falls below the peritectic temperature, the β-phase can nucleate, and coupled growth can be established on a much shorter timescale. Therefore, coupled growth takes place in a large-scale concentration field

that is the result of the ongoing growth transient, and that is still evolving with time. This concentration field is very different from the one associated with steady-state α–β-coupled growth [15]. We will see that this has a profound effect on the resulting microstructure.

To make these ideas more quantitative, a simple 1D model was used to solve the diffusion equation in the liquid, together with the evolution of the interface temperature (or, equivalently, position) for an α-liquid interface. The model takes into account the actual shape of the Cu–Sn solidus and liquidus curves, and solidification shrinkage (which turns out to have a much smaller effect). Once the interface reaches the peritectic temperature, a coupled growth mode is modeled by fixing the temperature of the interface, while the volume fraction is obtained from the interfacial solute flux. This model reproduces the slow decrease of g_α with time well, and correctly captures the high values of g_α observed in the experiments.

The rapid oscillations in g_α were analyzed with the help of a 2D quantitative multi-phase-field model that was initialized with the concentration field obtained from the 1D diffusion model. The phase-field model predicts a collective 1-λ oscillation of the lamellar structure (that is, the width of all β lamellae oscillate in phase), which is consistent with the observed oscillations in g_α. The control parameters and the lamellar spacing were then systematically varied to study their influence on the emergence of coupled growth. There is only a limited range of these parameters that produce stable two-phase microstructures. Outside this range, the simulations predict that one of the phases completely overgrows the other. The role of the diffusion coefficient D_ℓ, which is an important parameter that is not known to great precision, is also examined.

The remainder of the article is organized as follows: we first recall the experimental setup, and present results for a sample that was withdrawn at $v_p = 0.38$ μm s^{-1} (as compared to $v_p = 0.58$ μm s^{-1} in our previous work). Next, in Section 3, we present the 1D diffusion model and discuss its predictions for the evolution of g_α. The multi-phase-field model is briefly described in Section 4, and detailed simulation results are presented in Section 5. A brief discussion concludes the paper.

2. Experiments

The experimental results reported herein were obtained with the same apparatus and experimental methods as described by Kohler et al. [11] and Valloton et al. [18]. We therefore limit the description here to the essentials, and refer the interested reader to the previous articles. The sample was approximately 80 mm long and encapsulated in a 500 μm diameter capillary tube, which was first equilibrated in a fixed temperature gradient, and then withdrawn at a constant pulling speed of $v_p = 0.38$ μm s^{-1}. Thermocouple measurements showed that the thermal profile was linear between 450 and 1000 °C, and its value at the peritectic temperature (798 °C) was $G_\ell \approx 21$ K mm^{-1}.

After some time, the sample was quenched to capture the solid–liquid interface during solidification. The sample was then removed from the capillary and examined using ex situ X-ray tomography, optical microscopy and EBSD analysis. An example of the resulting microstructure is given in the longitudinal section shown in Fig. 1, showing both an optical micrograph and an EBSD false color orientation map. Computational models of the solidification showed that thermosolutal buoyancy should be suppressed in the 500 μm diameter capillary tube. These results are consistent with the flat quenched interface seen at the far right end of the sample. The length of the Bridgman solidified part of the sample was about 12 mm, leaving about 45 mm in the liquid ahead of the quenched interface. Since this distance is much greater than the diffusion length ($D_\ell/v_p \approx 10$ mm), we are confident that the microstructure was produced in an effectively semi-infinite diffusive regime.

On the left side of Fig. 1 (region (a)), we see the last part of the initial transient of the primary α-phase. In region (b), the first appearance of the β-phase seems to be highly unstable: we see a disordered pattern of α domains in a β matrix. The fact that most of these domains have the same orientation as the initial α phase in the EBSD analysis indicates that the α domain is in reality continuous in three dimensions, and that α and β undergo a competitive dynamics with successive overgrowth, as already observed in the early stages of eutectic coupled growth by Akamatsu et al. [20] in eutectics and by Kohler et al. [11] in peritectic coupled growth. The system then switches back to α before initiating coupled growth in region (c). The presence of multiple grains in this region, as seen on the EBSD map, suggests that some nucleation may have taken place ahead of the interface. However, we do not have a complete explanation.

Prior to cutting and polishing the specimen to obtain the micrographs shown in Fig. 1, X-ray microtomographic analysis was carried out at the European Synchrotron Radiation Facility on region (c), the zone of coupled growth. Fig. 2 shows selected reconstructed slices transverse to the pulling direction, spanning a distance of about 1.7 mm. One can clearly see the continuous lamellar structure along the length of the sample. Note that the variation in g_α appears as alternate thinning and thickening of the lamellae, and that we do not see the lamellae breaking up into fibers in this sample, as we did in the sample solidified at $v_p = 0.58$ μm s^{-1} described in Ref. [18]. The lamellar spacing over the whole coupled region was estimated by making 60 measurements along the length of the coupled zone, and then averaging them to obtain an approximate lamellar spacing of $\lambda = 45 \pm 4$ μm. We note that the lamellae grow at an angle to the pulling direction. This is probably due to a Kurdjumov–Sachs orientation relationship between the α and β phases [18]. The growth angle was not accounted for in the measurement of lamellar spacing.

Fig. 3 shows the variation of g_α with distance from the quenched interface, defined as $z' = 0$. Segmentation of the slices corresponding to the onset of coupled growth was unsuccessful due to the presence of noise and to the small size of the first peritectic regions. For this reason, the profile does not start at $g_\alpha = 1$ but rather at $g_\alpha \approx 0.6$. Note that one would expect $g_\alpha = 0.12$ for this composition from the equilibrium phase diagram, i.e. using the lever rule. As solidification proceeds, the average value of g_α, as indicated by the linear regression in Fig. 3, slowly decreases, reaching a value of about 0.5 at the time of the quench. The oscillations in $g_\alpha(z')$ correspond to the thinning and thickening of the lamellae shown in Fig. 2, whose positions are indicated as open circles. Since the α-lamellae thicken when the β-lamellae get thinner, and vice versa, the initial stage of peritectic growth exhibits 1-λ oscillations similar to those reported for eutectic alloys [21] as well as for Fe–Ni [10]. The additional curves in Fig. 3 will be explained later in Section 3.2.

3. Diffusion model

3.1. 1D model of the initial transient

We consider the directional solidification of primary α in one dimension with a planar front, pulled through a fixed temperature gradient G_ℓ at constant pulling velocity v_p. We make the following assumptions:

1. the process is 1D and semi-infinite in extent;
2. the temperature field is undisturbed by the movement of the interface;

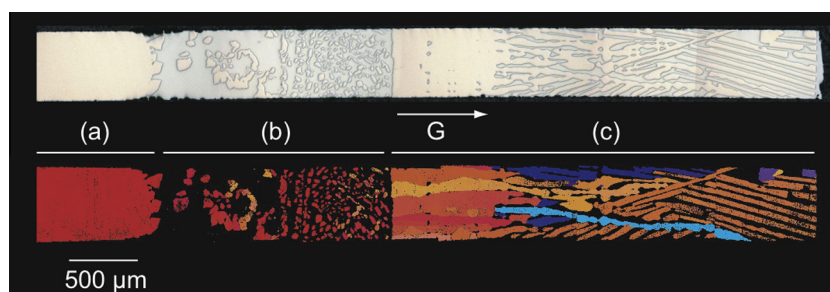Fig. 1. Optical (top) and EBSD (bottom) micrographs of a longitudinal section of a Cu–21 wt.% Sn sample solidified at $v_p = 0.38$ μm s^{-1} in a temperature gradient $G_\ell = 21$ K mm^{-1}. A region (a) of primary α at the far left gives way to a region (b) consisting of islands of α in a β matrix, which then returns to primary α. This is followed by region (c), where α and β grow in coupled form.
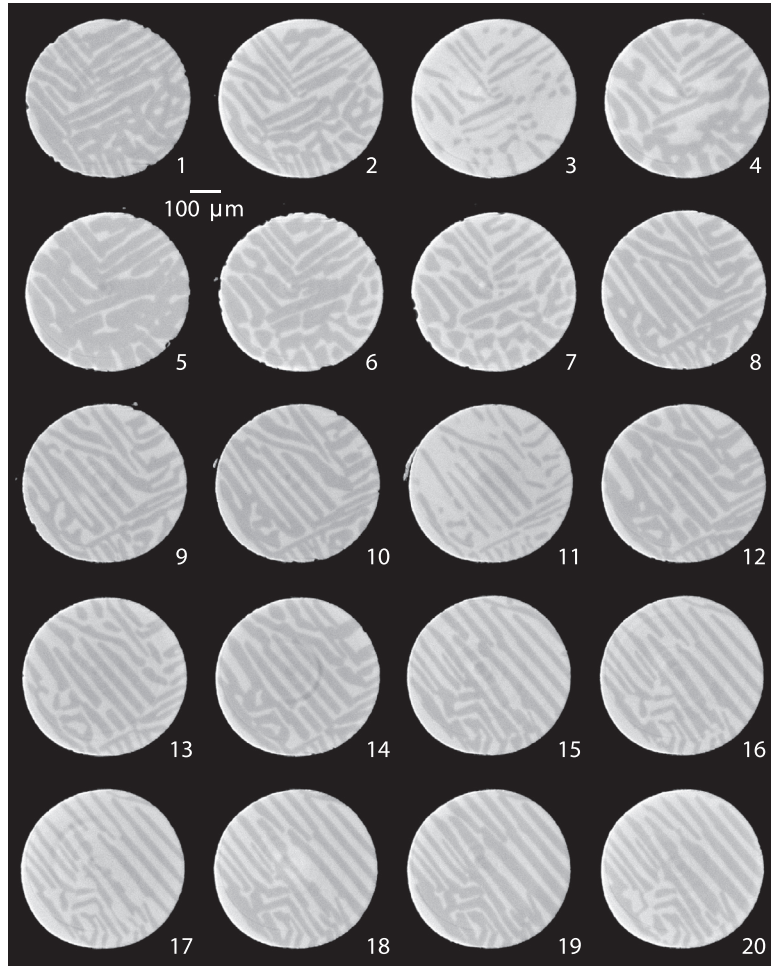
Fig. 2. Selected reconstructed slices perpendicular to the thermal gradient G_ℓ obtained by X-ray microtomography in the zone of coupled growth of the specimen shown in Fig. 1 (dark gray: α, light gray: β). The positions and volume fractions of each slice are highlighted in Fig. 3.
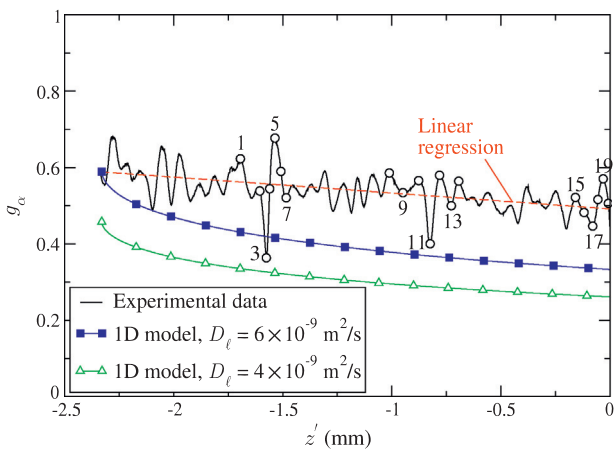

Fig. 3. Evolution of the volume fraction of the primary phase g_α in the region of coupled growth in the specimen shown in Fig. 1. g_α was determined directly from 3D X-ray microtomography. $z' = 0$ denotes the position of the quenched solid–liquid interface. The open circles correspond to the numbered transverse slices shown in Fig. 2. The linear regression fit to the values of g_α shows the gradual decrease with distance along the sample axis. The curves labeled "1D model" are explained in Section 3.2.

3. local equilibrium applies at the interface (note that this implies that the partition coefficients k_α and k_β cannot be constant because the corresponding liquidus and solidus curves are not straight lines);

4. diffusion in the solid is negligible, i.e. $D_s \ll D_\ell$;

5. the solid and liquid densities, ρ_s and ρ_ℓ, are constant, but unequal. This results in a flow towards the interface characterized by the shrinkage coefficient $\beta_s = \rho_s/\rho_\ell - 1$.

The calculations are carried out in a reference frame fixed on the solid–liquid interface, defined as $\zeta = 0$. The governing equation, boundary and initial conditions are given by

$$\frac{\partial C_\ell}{\partial t} - (1 + \beta_s)v^* \frac{\partial C_\ell}{\partial \zeta} = D_\ell \frac{\partial^2 C_\ell}{\partial \zeta^2} \quad 0 \leqslant \zeta < \infty \tag{1}$$

$$-\rho_\ell D_\ell \frac{\partial C_\ell}{\partial \zeta} = \rho_s C_\ell^*(1 - k_\alpha)v^* \qquad \zeta = 0 \tag{2}$$

$$C_\ell = C_\ell^* = C_{liq}^\alpha(T(\zeta)) \qquad \zeta = 0 \tag{3}$$

$$C_\ell = C_0 \qquad \zeta \to \infty \tag{4}$$

$$C_\ell = C_0 \qquad \zeta > 0, t = 0 \tag{5}$$

where v^* is the velocity of the interface relative to the end of the sample. Note that $v^* = 0$ at $t = 0$, and gradually increases until it reaches $v^* = v_p$ at steady state. The nominal composition of the alloy is C_0, $C_\ell(\zeta, t)$ is the composition profile in the liquid, and $C_{liq}^\alpha(T)$ is the liquidus of the α-phase.

This is a generalization of the well-known solution of Smith et al. [19], who, in order to obtain an analytical solution, made the additional assumptions that $v^* = v_p$ (which implies that the interface is stationary in the laboratory frame), k_α is constant and that $\beta_s = 0$. Note that these assumptions are inconsistent with Assumption 3 above, because the interface temperature must decrease as solidification proceeds to maintain local equilibrium at the interface. This implies in turn that the interface speed must be different from the pulling speed. Similar models have been developed previously. Mollard and Flemings [22] examined the initial transient in off-eutectic coupled growth by coupling Smith's solution for the primary phase solidification to a numerical method for the coupled growth region. Warren and Langer [23] constructed an approximate solution that accounted for the recoil of the interface, and Caroli et al. [24] solved the full dynamical equations numerically, finding similar results to Warren and Langer. None of these authors considered non-constant k_α, which we will see is very important for our alloy.

We developed a 1D finite difference code to satisfy the more general form of the equations, using the solution of Smith et al. as a verification. The calculation begins with the initial condition from Eq. (5). The temperature of the solid–liquid interface is computed, which determines the composition at the interface according to the digitized phase diagram. The composition field in the liquid after one time step is computed from Eq. (1), then the interface velocity is computed via Eq. (2). Finally, the updated interface velocity is used to compute the new interface position and temperature. This process is then repeated until the interface temperature reaches the peritectic temperature.

Fig. 4 shows results from the model corresponding to the experimental conditions: $v_p = 0.38$ μm s^{-1}, $G_\ell = 21$ K mm^{-1}, and with $D_\ell = 6 \times 10^{-9}$ m^2 s^{-1}. We plot the composition in the solid and liquid at the interface from the initial position, defined as $z = 0$, up to the position where the interface temperature reaches the peritectic temperature, defined as $z = z^*$. At this final position, we also show the composition in the liquid. In order to highlight the importance of the new phenomena included in the model, we show results for several cases, as the various phenomena are added one at a time (first $v^* \neq v_p$, then adding solidification shrinkage, and finally including non-constant k_α), and compare them to the solution of Smith et al. One can see that solidification shrinkage plays a relatively minor role, whereas the variable partition coefficient (i.e. including the actual shape of the phase diagram) has a very significant effect on the solute profile.

Fig. 4. Comparison of the evolution of the interface compositions C_α^* and C_ℓ^* during the initial transient. $C_0 = 21$ wt.% Sn, $v_p = 0.38$ μm s^{-1}, $G_\ell = 21$ K mm^{-1}, $D_\ell = 6 \times 10^{-9}$ m^2 s^{-1}.

3.2. 1D model for coupled growth

The transient model of the preceding section was used to generate the initial solute profile in the liquid ahead of the interface at the beginning of coupled growth. We ignore nucleation and initial spreading of the β-phase on the primary α-phase, and assume that coupled growth begins when the interface temperature reaches the peritectic temperature, and that the liquid composition at the interface $C_\ell(z^*)$ is equal to $C_\ell^{per} = C_\ell(T^{per})$. This event occurs after about 3 mm of growth of the primary phase, as shown in Fig. 4. At that instant, the solute profile in the liquid ahead of the interface has a very small negative slope, indicated by $dC_\ell/d\zeta$. The solute profile in the liquid predicted by the Smith solution is such that the thickness of the diffusion layer ahead of the interface is given by $D_\ell/v_p\Omega_\alpha(T^{per})$, where $\Omega_\alpha(T^{per}) = (C_\ell^{per} - C_0)/(C_\ell^{per} - C_\alpha^{per})$ is the supersaturation of the α-phase at the peritectic temperature, and C_ℓ^{per} and C_α^{per} are the liquid and α-phase compositions at T^{per}, respectively. The numerically computed solute profile in the liquid at this point was fitted to the following exponential form:

$$C_\ell^{IC}(z) = C_0 + (C_\ell^{per} - C_0) \exp\left(-\frac{F_{IC}v_p(z - z^*)}{D_\ell}\right) \quad (6)$$

where the factor F_{IC} is the single fitting parameter, and the subscript IC denotes that F_{IC} will be used to define the initial condition for the multi-phase field modeling presented in Section 4. Note that, when $F_{IC} = 1/\Omega_\alpha(T^{per})$, the Smith solution is retrieved. Also note that F_{IC} depends on G_ℓ, D_ℓ and v_p. For our experimental parameters, the numerical solution gives $F_{IC} = 1.928$, whereas $1/\Omega_\alpha(T^{per}) = 2.67$.

Since nucleation of the peritectic phase is not described by the phase field model we have used, it is necessary to set the initial volume fraction of the two solid phases. The solution of the 1D model of the initial transient is used to determine the value of $g_\alpha(t' = 0)$, where t' now refers to the time in the phase field calculation. Ignoring the

growth undercooling of the coupled $\alpha - \beta$ front (it will be shown to be very small), the solid–liquid interface now stays at the peritectic temperature and moves at the pulling velocity v_p. Setting the solute flux in the liquid equal to the rate of solute rejection by the moving interface, we can derive an expression for g_α at the onset of coupled growth:

$$-D_\ell \frac{\partial C_\ell^{lC}}{\partial z}\bigg|_{z=z^*} = v_p (C_\ell^{per} - \overline{C}) \tag{7}$$

$$-D_\ell (C_\ell^{per} - C_0)\frac{-F_{IC}v_p}{D_\ell} = v_p \left[C_\ell^{per} - \left(g_\alpha C_\alpha^{per} + (1-g_\alpha)C_\beta^{per} \right) \right] \tag{8}$$

$$\Rightarrow \quad g_\alpha = \frac{C_\beta^{per} - C_\ell^{per} + (C_\ell^{per} - C_0)F_{IC}}{C_\beta^{per} - C_\alpha^{per}} \tag{9}$$

where $\overline{C} = g_\alpha C_\alpha^{per} + (1-g_\alpha)C_\beta^{per}$ is the mean composition of the lamellar front at the solid–liquid interface and C_β^{per} is the solidus composition of β at T^{per}. This procedure is valid when the solute boundary layer does not vary significantly during the first stage of nucleation and growth of the peritectic phase.

There are two extreme cases of note. For the Smith solution, $F_{IC} = 1/\Omega_\alpha(T^{per})$ gives $g_\alpha^{Smith} = 1$. In steady-state coupled growth, $F_{IC}(t) = 1$ and the lever rule is retrieved, i.e. $g_\alpha^{lever} = \left(C_\beta^{per} - C_0 \right)/\left(C_\beta^{per} - C_\alpha^{per} \right)$. Substituting the numerical values corresponding to the experimental conditions into Eq. (9) ($C_0 = 21$ wt.% and $F_{IC} = 1.928$) gives $g_\alpha = 0.61$, which is consistent with the experimental results shown in Fig. 3 and is much greater than the lever rule value, $g_\alpha^{lever} = 0.12$. This simple model shows that the unexpectedly high values of g_α at the start of coupled growth can be explained by considering the solute profile that develops during the solidification of the α-phase, which is not yet that of the steady-state solution for coupled growth.

During coupled growth, the interface temperature remains close to T_{per}, and thus the interface moves at constant speed v_p. In that case, $C_\ell(\zeta, t)$ evolves according to Eq. (1) with $v^* = v_p$, and Eq. (3) is replaced by $C_\ell(\zeta = 0) = C_\ell^{per}$. Since the temperature, liquid composition and velocity of the interface are now known, Eq. (2) is no longer needed, and is instead replaced by an equation similar to Eq. (7), in which the solute gradient at the interface is obtained numerically at each time step, and the unknown is g_α. The initial condition is given by Eq. (6) instead of Eq. (5). This new system of equations can be readily solved numerically. The results, corresponding to the experimental parameters and two different values of the diffusion coefficient, are also plotted in Fig. 3 (marked "1D solution"). One can see that although the general trend is similar, this simplified model tends to overestimate the rate at which $\bar{g}_\alpha$ decreases. This is probably because our analysis begins after the coupled growth has been established, rather than at the initial appearance of β-phase, where $g_\alpha = 1$. Nevertheless, this model has the merit of providing an explanation for why g_α goes from one at the time of nucleation of β to the lever rule value at steady state. This is due to the evolution of the solute profile in the liquid

which, according to the Smith solution, is characterized by a diffusion layer thickness $\Omega_\alpha(T^{per})D_\ell/v_p$ at the onset of coupled growth, and by D_ℓ/v_p at steady state.

4. Multi-phase field modeling

The simple 1D models presented in Sections 3.1 and 3.2 help to explain some of the phenomena observed in the experiments. The oscillations in g_α, however, are linked to the time evolution of the microstructure and thus require a more detailed model. We use the multi-phase field model developed by Folch and Plapp [25], since it has been extensively validated for eutectic alloys. Whereas this model was originally designed for the modeling of eutectics, it can be used for peritectics without difficulty by changing the phase diagram parameters. All details of the model are given in Ref. [25], so are not repeated here.

The code was modified to take into account the findings discussed in the preceding section: the calculations begin with the interface at the peritectic temperature T_{per} and the concentration field in the liquid given by Eq. (6). The region $T < T_{per}$ contains the solid phases, in the proportion given by Eq. (9), and with initial compositions C_α^{per} and C_β^{per}, respectively. For the geometry of the two solid phases, we considered two different configurations:

- $\lambda/2$ *configuration*: Two half-lamellae with their respective centers on the sides of the simulation box. This is the minimal configuration for simulating a periodic lamellar array. The center-line of each lamella corresponds to a mirror symmetry plane of the lamellar structure, and therefore the application of reflecting boundary conditions along these lines make the solution equivalent to an infinite periodic array. The simulation was started from two rectangular domains of the two phases, with the α-liquid interface usually starting slightly ahead of the β-liquid interface.
- 4λ *configuration*: Four lamellae of each phase with eight triple junctions. To test the stability of the lamellar array against lamella elimination, small perturbations in the width and the starting position of the solid–liquid interface were added.

A multigrid approach is used for the numerical solution of the governing equations in order to resolve the wide range of important physical and computational length scales. The diffuse interface width W for the phase-field variables must be small compared to the radius of curvature of the interface, which is of the order of the lamellar spacing λ; the grid spacing Δx must be small enough to resolve the interface ($\Delta x \lesssim W$); the short-range 2D diffusion field ahead of the interface, $\mathcal{O}((3-5)\lambda)$, and the long-range 1D diffusion field, $\mathcal{O}((3-5)D_\ell/v_p)$, must both be independent of the grid and size of the computational domain.

Several simulations were performed in order to determine computational parameters that gave converged

results. This was achieved for $\Delta x = \lambda/128$. Choosing the interface width $W = 1.25\Delta x$ ensured that the diffuse interface was fully resolved, and computational examples showed that the interface curvature was adequately resolved. The 2D mesh layering scheme for these parameter choices covers a distance of about 4λ in the pulling direction with a 2D grid. The remaining long-range diffusion tail is resolved with a 1D grid extending another $5D_\ell/v_p$.

The calculations were carried out in scaled form. Length was scaled on the diffuse interface width W, and the minimum grid spacing in scaled coordinates is then $\Delta \tilde{x} = 0.8W$. The timescale is a bit more complicated. We first define the ratios

$$U_\alpha = \frac{C_\alpha^{per} - C_\ell^{per}}{C_\beta^{per} - C_\alpha^{per}}; \quad U_\beta = \frac{C_\beta^{per} - C_\ell^{per}}{C_\beta^{per} - C_\alpha^{per}} \quad (10)$$

The tilt parameter in the definition of the phase field free energy (see Ref. [25]) $\tilde{\lambda} = 2\sqrt{2}/(3Wd_\alpha|U_\alpha|)$ where $d_\alpha = \Gamma_\alpha T_{per}/\left(m_{\ell\alpha} T_f^\alpha \left(C_\beta^{per} - C_\alpha^{per}\right)\right)$ is the capillary length for phase α, Γ_α the corresponding Gibbs–Thomson parameter, $m_{\ell\alpha}$ the slope of the α liquidus and T_f^α is its melting point. We then define a timescale as a mean relaxation timescale for each phase, $\bar{\tau} = 0.3732\tilde{\lambda}W^2(U_\alpha^2 + U_\beta^2)/D_\ell$. All of the physical parameters can now be scaled using W and $\bar{\tau}$. In particular, $\tilde{D} = D_\ell\bar{\tau}/W^2$. The time step size is then set to ensure stability, $\Delta \tilde{t} \leqslant 0.25\Delta \tilde{x}^2/\tilde{D}$.

Because the interface temperature during coupled peritectic growth at low solidification speed remains close to the peritectic temperature T_{per}, it is a reasonable approximation to consider the liquidus and solidus phase boundaries in the equilibrium phase diagram to be straight and parallel lines. Also, at low solidification speeds the kinetic undercooling can be ignored. Finally, we take the surface energy for all interfaces to be equal, implying equal angles between each two binary interfaces at the triple junction. The parameters used in the phase-field model are summarized in Table 1.

Table 1
Computational parameters for the phase-field modeling of coupled growth.

Parameter	Symbol	Value	Unit
Nominal composition	C_0	21	wt.%
Lamellar spacing	λ	25–70	μm
Liquidus slope of α	$m_{\ell\alpha}$	−11.03	K/wt.%
Liquidus slope of β	$m_{\ell\beta}$	−5.53	K/wt.%
Peritectic temperature	T_{per}	1068.9	K
C_α at T_{per}	C_α^{per}	13.5	wt.%
C_ℓ at T_{per}	C_ℓ^{per}	25.5	wt.%
Peritectic composition	C_β^{per}	22	wt.%
Diffusion coefficient	D_ℓ	$3 - 7 \times 10^{-9}$	m²s⁻¹
Thermal gradient	G_ℓ	21–35	K mm⁻¹
Pulling velocity	v_p	0.38–0.58	μm s⁻¹
Partition coefficient at T_{per}, α	k_α	0.53	–
Partition coefficient at T_{per}, β	k_β	0.86	–
Gibbs–Thomson coefficient, α	Γ_α	3×10^{-7}	K m
Gibbs–Thomson coefficient, β	Γ_β	3×10^{-7}	K m

5. Results and discussion

5.1. Base case

We present first (in Fig. 5) the results of a simulation using the 4λ configuration. For this case, we use $\lambda = 45$ μm, and $D_\ell = 6 \times 10^{-9}$ m²/s. The remaining parameters are as listed in Table 1.

Several important features of the microstructure evolution can be seen. The volume fraction g_α oscillates with a spatial period approximately equal to the lamellar spacing λ. The initial perturbations in spacing are damped out rather quickly as growth proceeds. The nearly horizontal curves in the figure represent successive locations of the interface at equally spaced time intervals. One can see that as g_α increases the interface speed decreases (curves come closer together), and as g_β increases the interface accelerates (curves become further apart). Note also that both phases accelerate or decelerate together. This is different from the 1-λ oscillations observed in eutectics, where one usually finds that when the solid–liquid interface of one phase accelerates the solid–liquid interface of the other phase decelerates.

We repeated this simulation in the $\lambda/2$ configuration. All the parameters were the same, except that for this geometry there is no perturbation possible in lamellar spacing. The result is summarized in Fig. 6, where we compare the computed evolution of g_α for the two configurations.
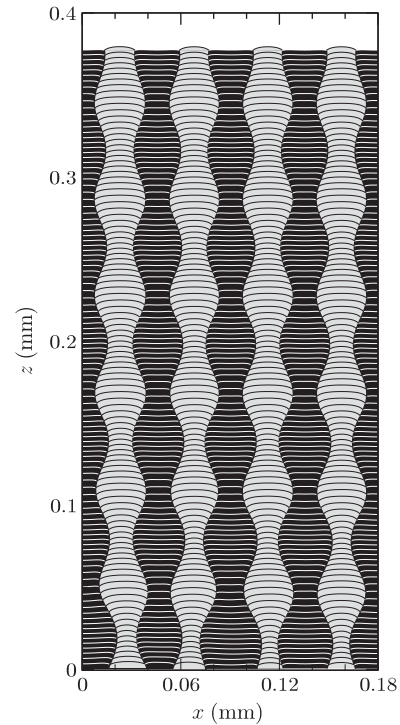

Fig. 5. Computed microstructure for 4λ configuration. The black, gray and white regions represent the α, β and liquid phases, respectively. The nearly horizontal lines correspond to interface positions at equally spaced time intervals.

One can see that the results are nearly identical. The small difference in g_α is due to the fact that the perturbation in spacing in the 4λ case slightly changes the volume fraction of the phases. Given these results, and the fact that the simulations for the $\lambda/2$ configuration run about 50 times faster than those for the 4λ case, the remainder of the results presented below were obtained using the $\lambda/2$ configuration. We also show the expected value of $\bar{g}_\alpha$ from the model of Section 3.2. The phase field results track the 1D model very well. Note that the total range of z in Fig. 6 is much smaller than in Fig. 3. The computed solute field in the liquid over the fourth cycle in the $\lambda/2$ configuration simulation is shown in Fig. 7.

The spatial period of the oscillation is about 60 μm, which corresponds to an elapsed time of about 160 s. The solute gradient in the liquid is mainly perpendicular to the solid–liquid interface, since both phases reject tin, but with a small component parallel to the interface going from the α-phase to the β-phase as in the peritectic reaction.

The evolution of the temperature of the solid–liquid interface during the cycle is shown in Fig. 8. Initially (snapshot 1), both α-liquid and β-liquid interfaces are located partly above and partly below the peritectic temperature, with the triple junction below T_{per}. At the beginning of the cycle, g_α increases. Since $k_\alpha < k_\beta$, the average liquid composition ahead of the lamellar front increases and accordingly the temperature of the front decreases. When the center of the β-lamella reaches a temperature about 0.02 K below T_{per}, the undercooling is sufficient to enable a rapid increase of $g_\beta = (1 - g_\alpha)$ at nearly fixed undercooling, while the temperature of the α-lamella decreases further (snapshot 9). Since the peritectic phase rejects less solute than the primary phase, the liquid composition at the interface then decreases and the temperature increases. As the temperature of the peritectic phase crosses T_{per}, g_β then recedes slightly. When the temperature of the primary phase finally rises again above T_{per}, g_α rapidly increases in turn at nearly constant temperature and the cycle begins
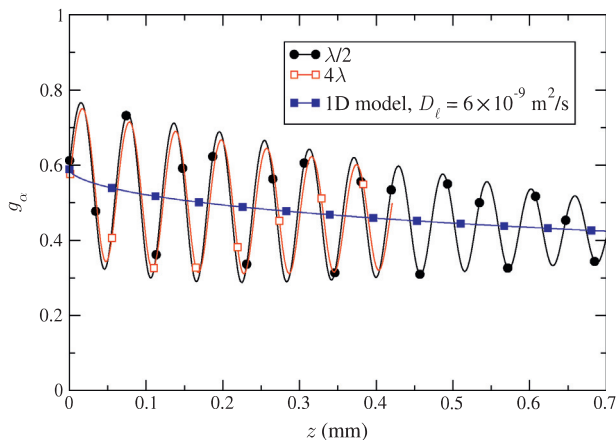
anew (snapshot 18). Note that as the interface temperature falls the interface speed decreases (because G_ℓ and v_p are fixed), and the converse applies when the interface temperature increases. Note also that because the amplitude of the oscillation is decreasing with time, the trajectory of the triple point, shown in blue in Fig. 8, forms a loop that does not close.

Let us now look more closely at the details of the interface temperature and composition during one cycle of the oscillation in g_α. Since the temperature $T^*(x)$ of the solid–liquid interfaces is known from the calculation, the local liquid composition along the interface ahead of α and β, $C_\ell^{*\alpha}(x)$ and $C_\ell^{*\beta}(x)$ respectively, can be computed from the Gibbs–Thomson relation:

$$C_\ell^{*v}(x) = C_\ell^{per} + \frac{\Gamma_{s\ell}K(x) + T^*(x) - T_{per}}{m_{\ell,v}} \qquad v = \alpha, \beta \quad (11)$$

where $K(x)$ is the local curvature of the interface, calculated as:

$$K(x) = -\frac{\partial_{xx}z^*}{\left[1 + (\partial_x z^*)^2\right]^{3/2}} \quad (12)$$

where $z^*(x)$ is the position of the solid–liquid interface in the moving reference frame. Note that the concentrations at the interfaces cannot be directly obtained from the phase-field model with sufficient precision because of the smeared-out solute redistribution inside the interfaces. Fig. 9 shows the operating temperatures and liquid compositions of the lamellar structures of snapshots 9 and 16 from Fig. 7, computed via Eq. (11), superimposed on the phase diagram near T_{per}. Because of the interface curvature, the liquid can have the same composition but be at different temperatures. In both snapshots, the liquid composition in front of the primary phase is larger than that in front of the peritectic phase, even when the front is completely below T_{per}, so that diffusion always goes from α to β, as already pointed out.

There has been considerable debate concerning the temperature of a peritectic coupled growth front. The theory of Jackson and Hunt for regular eutectic alloys [26] was extended by Boettinger to peritectic alloys [15]. The main result of his analysis is that, for a small g_α at steady state (i.e. C_0 close to C_β^{per}), the undercooling of the lamellar front (assumed isothermal) is always negative (superheating), regardless of the lamellar spacing. In their simulations of the Fe–Ni system, Dobler et al. found that this theory does not accurately describe the interface temperature, and that the interface temperature was very close to the peritectic temperature. Lee and Verhoeven [27] reported in a study of Ni-Al alloys that the coupled solid–liquid interface was isothermal and slightly below the peritectic temperature, whereas Vandyoussefi et al. [28] in Fe–Ni alloys, and Su et al. [13] in Cu–Sn alloys found that the lamellar front was isothermal, but slightly above T_{per}.

In the simulations discussed so far, steady-state peritectic coupled growth was never reached. To explore
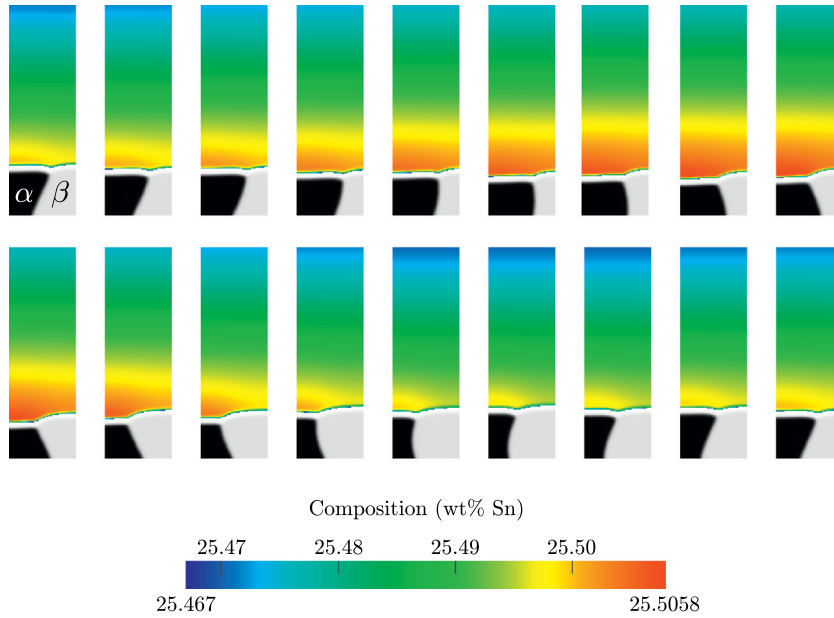

Fig. 6. Evolution of the volume fraction g_α for the base case parameters, in the 4λ and $\lambda/2$ configurations.

Fig. 7. Snapshots of the composition field in the liquid during one oscillation of the $\alpha + \beta$ front ($C_0 = 21$ wt.% Sn, $\lambda = 45$ μm, $D_\ell = 6 \times 10^{-9}$ m² s⁻¹, $v_p = 0.38$ μm s⁻¹, and $G_\ell = 21$ K mm⁻¹). The period of the oscillation of g_α is 55–60 μm.
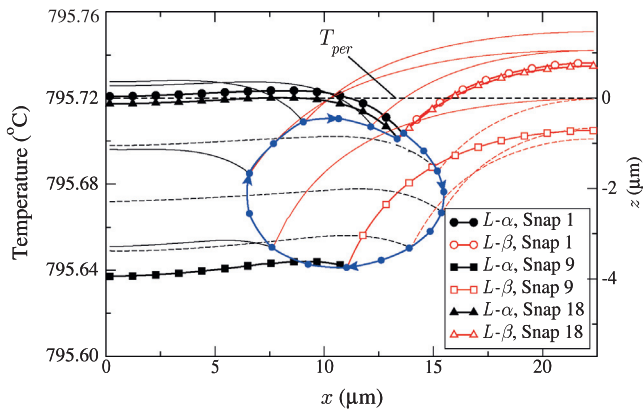

Fig. 8. Evolution of the interface temperature during one oscillation. The trajectory of the triple point is shown in blue. Note that the vertical length scale, converted from the temperature using G_ℓ, is magnified in comparison to the horizontal scale.
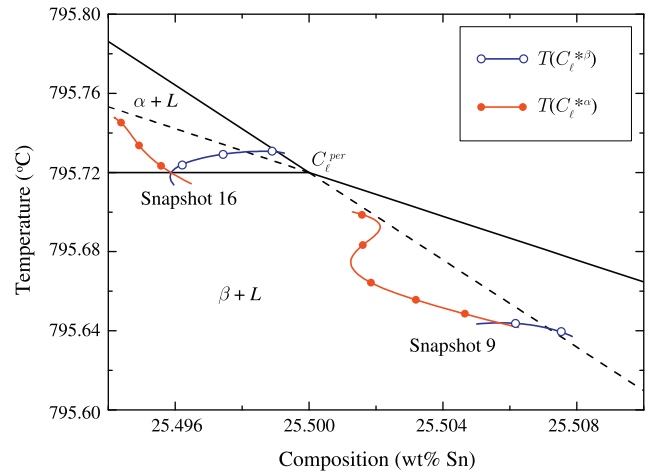
Fig. 9. Operating temperatures of the lamellar structures seen in snapshots 9 and 16 of Fig. 7 superimposed on the phase diagram.

steady-state growth, a simulation was performed beginning with $F_{IC} = 1.04$, i.e. close to steady state. The volume fraction obtained after stabilization, $g_\alpha = 0.110$, is very close to the equilibrium fraction defined by the lever rule, $g_\alpha^{lever} = 0.118$. As can be seen in Fig. 10, the lamellar front at steady state is not strictly isothermal, as previously noted by Kohler [29]. The temperature of the α-lamella is located below T_{per}, whereas that of the β-lamella crosses the peritectic temperature; the temperature of the triple junction is always below the peritectic temperature (see Fig. 9). In any case, the temperature differences along the interface and between the interface and the equilibrium peritectic temperature are very small (<0.1 K, see Fig. 9). Such temperature differences are extremely difficult to measure, and therefore the question of whether the interface observed in

the experiments is really above or below the peritectic temperature is quite undecidable, especially if one considers the uncertainty of the phase diagram itself. These observations also can explain why the Jackson–Hunt–Boettinger theory cannot be accurate. This theory works with the average undercooling of the interfaces. Here, the variations of the local undercooling within the β phase are of the same order of magnitude as the total undercooling itself, so that the validity of this averaging procedures must be questioned.

The coupling between the variations of g_α and the average interface velocity v^* can be explained by looking at the average solute balance at the interface. If we approximate the solute gradient in Eq. (7) by $-(C_\ell^{per} - C_0)/\delta$, we have

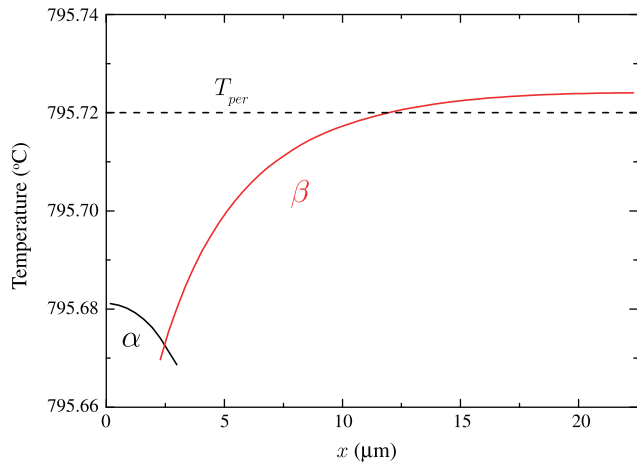$$D_\ell \frac{C_\ell^{per} - C_0}{\delta} = v^* C_\ell^{per}[(1 - k_\alpha)g_\alpha + (1 - k_\beta)(1 - g_\alpha)] \quad (13)$$

Fig. 10. Temperature of the interface at steady state. The volume fraction of α is very close to g_α^{lever}.

Differentiating Eq. (13) with respect to time gives

$$-D_\ell \frac{C_\ell^{per} - C_0}{\delta^2} \frac{d\delta}{dt} = \frac{dv^*}{dt} C_\ell^{per} \left[(1 - k_{0\alpha})g_\alpha + (1 - k_{0\beta})(1 - g_\alpha)\right]$$
$$+ v^* C_\ell^{per}(k_\beta - k_\alpha) \frac{dg_\alpha}{dt} \tag{14}$$

The time required for solute to diffuse over the extent of the initial boundary layer, $\delta^2/D_\ell \approx D_\ell/v_p^2 \approx 40,000$ s, is much larger than the period of the microstructural oscillations in g_α (160 s). Thus, on the latter timescale the left-hand side of Eq. (14) can be set to zero. The coefficients of dv^*/dt and dg_α/dt on the right-hand side of Eq. (14) are both always positive since k_α and k_β are positive, and $k_\alpha < k_\beta$. Thus, when the interface decelerates ($dv^*/dt < 0$), the volume fraction of the primary phase increases ($dg_\alpha/dt > 0$), and conversely when $dv^*/dt > 0$, as observed in Fig. 5.

5.2. Parameter variation and stability limits

The stable oscillatory microstructures described in the preceding section occur only over a limited range of the parameters. In this section, we investigate the behavior as v_p, G_ℓ, λ and D_ℓ vary. The latter is of course a physical parameter that does not vary in practice, but its value is not known to great precision. Thus, varying D_ℓ measures the sensitivity of the results to this parameter. We choose as our base values the parameters for which we have already presented results, i.e. $v_p = 0.38$ μm s^{-1}, $G_\ell = 21$ -K mm^{-1}, $\lambda = 45$ μm and $D_\ell = 6 \times 10^{-9}$ m^2 s^{-1}, and then perform simulations in which one of these parameters is varied.

Fig. 11 shows the evolution of the volume fraction g_α as the lamellar spacing is varied. The experimentally measured volume fraction determined by X-ray microtomography for the sample solidified in these conditions is also shown. Stable microstructures are found for λ between 35 and 55 μm. Note that the experimental lamellar spacing determined for the corresponding sample falls into this range ($\lambda = 45 \pm 4$ μm). For spacings outside this range,

the amplitude of the oscillations increases over time until one phase completely overtakes the other.

Fig. 12 shows the evolution of g_α for various values of D_ℓ. Note that the initial value of g_α increases with D_ℓ, because the development of the initial transient also depends on D_ℓ, which in turn affects the factor F_{IC} via Eq. (9). We found a narrow range of values for D_ℓ that produce stable structures. Lower values of D_ℓ led to lamellar termination in β, whereas higher values of D_ℓ led to termination in α.

The effect of varying G_ℓ is shown in Fig. 13. Three different values of G_ℓ, 21, 25 and 35 K mm^{-1}, were chosen. Again, it can be seen that the initial value of g_α changes with G_ℓ. The reason is similar to the variation with D_ℓ, but slightly more complicated. During the initial transient of the α-planar front growth, the temperature of the interface recedes from $T_{\ell iq}^\alpha(C_0)$ to T_{per}, where $T_{\ell iq}^\alpha(C_0)$ is the liquidus of the primary phase. Therefore, the velocity of the α-liquid interface is lower than the actual pulling velocity. Increasing G_ℓ increases the velocity of the interface (if $G_\ell \to \infty$, $v^* \to v_p$), which increases F_{IC}, and in turn g_α. As expected, increasing G_ℓ from 21 to 25 K mm^{-1} stabilizes the microstructure. Indeed, the oscillations are damped more rapidly. Surprisingly, with a further increase to 35 K mm^{-1} the lamellar structure is no longer stable. This is probably due to the high initial value of g_α. Indeed, with an initial g_α close to 1, no oscillations are observed but the α-phase takes over straight away.

The results for the stability behavior in the simulations described above, and for an additional series of similar calculations for $v_p = 0.58$ μm s^{-1}, are summarized in Fig. 14, indicating where coupled growth is stable, or whether it becomes unstable to either α or β for a given pair of G_ℓ and λ. In order to present these results in a compact form, the lamellar spacing is scaled by the diffusion length D_ℓ/v_p
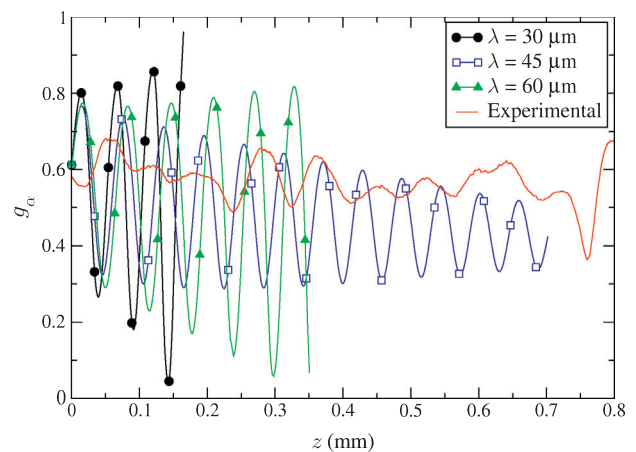

Fig. 11. Evolution of the volume fraction g_α for different lamellar spacings ($C_0 = 21$ wt.% Sn, $D_\ell = 6 \times 10^{-9}$ m^2 s^{-1}, $v_p = 0.38$ μm s^{-1} and $G_\ell = 21$ -K mm^{-1}). For small spacing, the coupled growth terminates in primary α, whereas for large spacing, coupled growth terminates in peritectic β. Intermediate spacings produce coupled growth, with decreasing amplitude oscillations.
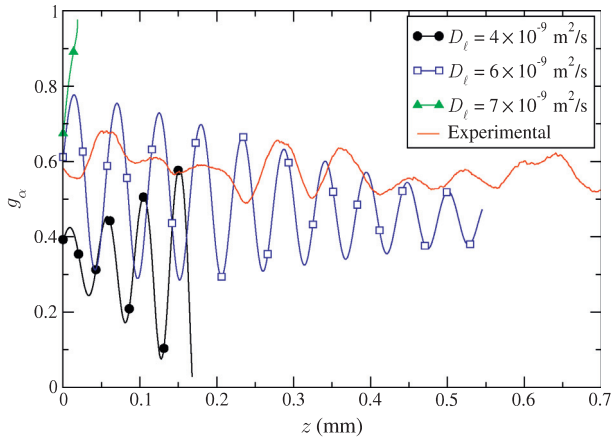
Fig. 12. Evolution of the volume fraction g_α for different diffusion coefficients ($C_0 = 21$ wt.% Sn, $\lambda = 35$ μm, $v_p = 0.38$ μm s^{-1}, and $G_\ell = 21$ K mm^{-1}).

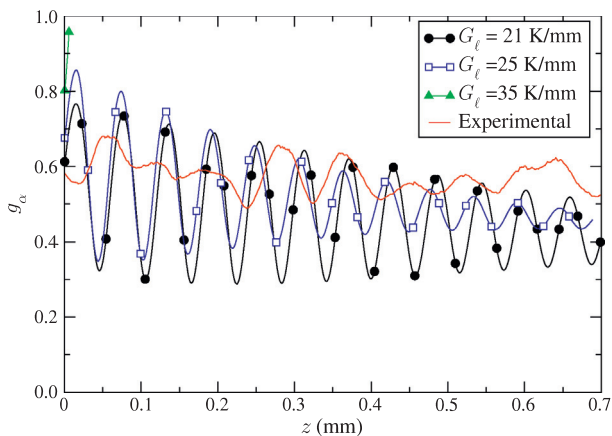Fig. 13. Evolution of the volume fraction g_α for different thermal gradients ($C_0 = 21$ wt.% Sn, $D_\ell = 6 \times 10^{-9}$ m^2 s^{-1}, $\lambda = 35$ μm and $v_p = 0.38$ μm s^{-1}).
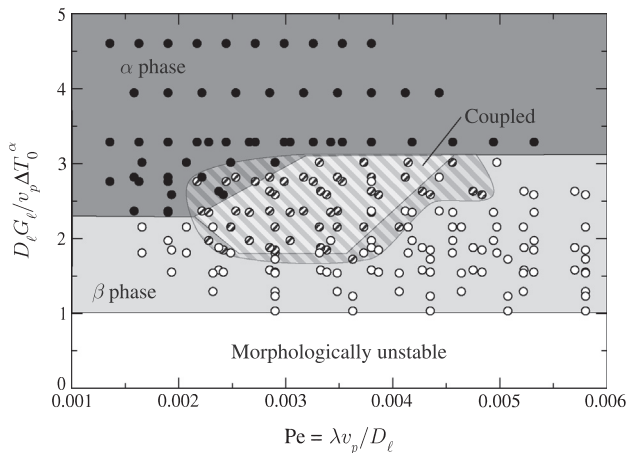
Fig. 14. Stability balloon for coupled growth for the various conditions examined in this study.

(i.e. Pe $= v_p\lambda/D_\ell$) and the temperature is scaled by ΔT_0^α. The ordinate then becomes the usual constitutional supercooling parameter $M = D_\ell G_\ell/v_p\Delta T_0^\alpha$, which must be greater

than one for the α planar interface to be morphologically stable in the absence of β. We find a central region of stable coupled growth with g_α slowly converging towards the lever rule, surrounded by conditions that lead to a diverging g_α and complete overgrowth by either the primary phase at high G_ℓ, or the peritectic phase at low G_ℓ. The region is defined roughly by $2 \leqslant M \leqslant 3$ and $0.002 \leqslant$ Pe $\leqslant 0.004$.

We can explain the limited range of stability of coupled growth by examining the value of g_α when the initial primary phase transient switches to a coupled growth mode. At the start of all simulations, $g_\alpha(z)$ first increases, due to the initial composition profile in the liquid, which corresponds to the profile ahead of an α-planar front, favoring the growth of the primary phase. If the initial value of g_α is large enough, the oscillations terminate in the α phase. Similarly, for low enough initial values of g_α, the oscillations terminate in β instead.

The initial value of g_α comes from our 1D numerical model, which provides the initial solute profile. Changing the parameters G_ℓ, v_p and D_ℓ alter the solute diffusion field, which then changes g_α through Eq. (9). For example, when G_ℓ increases, the interface recedes a smaller distance to reach the temperature corresponding to local equilibrium, which thus increases the solute gradient, and in turn the initial value of g_α. The effect of D_ℓ is a little more complicated to unravel. As D_ℓ increases, the slope of the solute profile decreases, but not as rapidly as D_ℓ. This increases the value of F_{IC}, which again increases the initial value of g_α. This accounts for the lobes in the α and β zones terminating the coupled zone for $2 \leqslant M \leqslant 3$.

As a final remark, let us recall that our phase-field simulations are started from well-developed lamellae, with a volume fraction that is set by the solution of the macroscopic 1D problem. In reality, the coupled growth is initiated by the nucleation of the peritectic phase on a planar interface of the primary phase. The nucleus then spreads laterally over the interface, and lamellar growth emerges only much later. In view of this difference, we do not expect our simulations to be quantitatively correct. Phase-field simulations that include nucleation and spreading of the peritectic phase have been carried out in Refs. [8,30] for different phase diagrams. It was found that, depending on the pulling speed, the composition and the distance between nuclei (equivalent to the lamellar spacing), the peritectic phase can completely cover the interface, completely disappear after the formation of an "island" or develop into oscillating lamellae which evolve toward coupled growth. There is thus good overall agreement with our results, and therefore we believe that the results of Fig. 14 are at least qualitatively correct.

6. Conclusion

We have modeled the directional solidification of a hypoperitectic tin bronze with two different approaches: a macroscopic diffusion model and a multi-phase-field model for microstructure evolution. This combination of methods

has allowed us to cover a large range of lengths and time-scales (ranging from the microstructural to the macroscopic scales), and to carry out quantitative comparisons with experiments. The large volume fraction of primary phase found experimentally in the coupled structure is due to the solute profile in the liquid at the onset of peritectic coupled growth. A long transient is required to approach the steady-state solute boundary layer, and for the average composition of the solid to increase from C_α^{per} when only the primary phase is present to C_0 at steady state. This explains the slow decrease of g_α with increasing solidification distance. The oscillatory behavior of g_α is linked to a collective oscillation of the lamellar pattern (1-λ oscillations).

We expect the phenomena observed and modeled here to be fairly generic. The slow drift of the volume fractions with time is due simply to the slow pulling speed, which leads to a large diffusion length and a slow characteristic evolution time for the solute boundary layer. Since this slow speed is required to avoid morphological instabilities, such drifts should appear in all peritectic alloys that have a sufficiently large freezing range. This also implies that peritectic two-phase growth cannot be fully understood in terms of the basic steady-state solutions. It should be stressed that the scenario outlined in this work – a slow single-phase transient followed by coupled growth – is only a simplified model. Certain features observed in the experiments remain unexplained. For instance, our theory cannot account for the transition from two-phase back to one-phase growth at the borders between regions (b) and (c) in Fig. 1, because the theory contains no mechanism by which the interface temperature could rise above the peritectic temperature once two-phase growth has started. The history of this sample is thus more complicated than a simple 1D transient, which might explain the difference in the rates of change of g_α between experiments and simulations seen in Fig. 3.

The collective oscillations of the lamellar structure are also fairly generic. They are due to the complex interaction between the shape of the two-phase interface and the solute diffusion field. Such oscillations systematically occur in thin-sample eutectic growth close to the eutectic composition, and were also found in a few peritectic systems [8,31,30]. In agreement with the latter studies, we found that lamellar coupled peritectic growth is stable only in a narrow window of parameters. There is currently no theory available to predict these stability limits, and thus to predict whether for a given alloy and a set of growth conditions coupled peritectic growth will be observable. More work on the microstructural scale is necessary to make progress in this direction.

There is also one striking difference between these oscillations in eutectic and peritectic systems: the 3D tomographic data reported here clearly demonstrate that the collective $1 - \lambda$ oscillatory mode is relevant for peritectic coupled growth in 3D. In contrast, it was found both in experiments [32] and simulations [33] that, for eutectics, for bulk systems such oscillations are preceded by a zig-zag instability mode and are therefore never observed. Whether this difference is due only to the phase diagrams or whether crystallographic effects come into play remains to be elucidated.

References

[1] Trivedi R. Metall Mater Trans 1995;26A:1583.
[2] Kerr H, Kurz W. Int Mater Rev 1996;41:129.
[3] Trivedi R, Karma A, Lo T, Park J, Plapp M. Solidification microstructures. In: Proc. 2nd workshop Zermatt. Zermatt, Switzerland, 1998.
[4] Hunziker O, Vandyoussefi M, Kurz W. Acta Mater 1998;46:6325.
[5] Karma A, Rappel W, Fuh B, Trivedi R. Metall Mater Trans 1998;29A:1457.
[6] Boettinger W, Coriell S, Greer A, Karma A, Kurz W, Rappaz M, et al. Acta Mater 2000;48:43.
[7] Trivedi R, Park J. J Cryst Growth 2002;235:572.
[8] Lo T, Dobler S, Plapp M, Karma A, Kurz W. Acta Mater 2003;51:599.
[9] Dobler S. Solidification biphasée des alliages péritectiques Fe–Ni. PhD thesis, Ecole Polytechnique Fédérale de Lausanne, Switzerland, Lausanne, 2001.
[10] Dobler S, Lo T, Plapp M, Karma A, Kurz W. Acta Mater 2004;52:2795.
[11] Kohler F, Germond L, Wagnière JD, Rappaz M. Acta Mater 2009;57:56.
[12] Liu D, Li X, Su Y, Luo L, Zhang B, Fu H. Mater Lett 2011;65:1628.
[13] Su Y, Liu D, Li Z, Luo L, Guo J, Fu H. Metall Mater Trans A 2012;43A:4219.
[14] Chalmers B. Physical metallurgy. New York (NY): Wiley; 1959.
[15] Boettinger W. Metall Mater Trans 1974;5:2023.
[16] Mazumder P, Trivedi R. Phys Rev Lett 2002;88.
[17] Rappaz M, Kohler F, Valloton J, Phillion A, Stampanoni M. Metall Mater Trans 2010;41A:563.
[18] Valloton J, Wagnière JD, Rappaz M. Acta Mater 2012;60:3840.
[19] Smith V, Tiller W, Rutter J. Can J Phys 1955;33:723.
[20] Akamatsu S, Moulinet S, Faivre G. Metall Mater Trans 2001;32A:2039.
[21] Akamatsu S, Plapp M, Faivre G, Karma A. Metall Mater Trans 2004;35A:1815.
[22] Mollard FR, Flemings MC. Trans Metal Soc AIME 1967;239:1526.
[23] Warren JA, Langer J. Phys Rev 1993;E47:2702.
[24] Caroli B, Caroli C, Ramirez-Piscina L. J Cryst Growth 2003;132:377.
[25] Folch R, Plapp M. Phys Rev E 2005;72.
[26] Jackson K, Hunt J. Trans Metal Soc AIME 1966;236:1129.
[27] Lee J, Verhoeven J. J Cryst Growth 1994;144:353.
[28] Vandyoussefi M, Kerr H, Kurz W. Acta Mater 2000;48:2297.
[29] Kohler F. Peritectic solidification of Cu–Sn alloys: microstructure competition at low speed. PhD thesis, ♯ 4037, Ecole Polytechnique Fédérale de Lausanne, Switzerland, 2008.
[30] Lo T, Karma A, Plapp M. Phys Rev E 2001;63:031504.
[31] Dobler S, Kurz W. Z Metallkd 2004;95:592.
[32] Akamatsu S, Bottin-Rousseau S, Faivre G. PRL 2004;93:175701.
[33] Parisi A, Plapp M. Acta Mater 2008;56:1348.